Antimonide-based membranes synthesis integration and strain engineering

Marziyeh Zamiri[a,b,1], Farhana Anwar[a,b], Brianna A. Klein[c], Amin Rasoulof[b], Noel M. Dawson[a,b], Ted Schuler-Sandy[d], Christoph F. Deneke[e], Sukarno O. Ferreira[f], Francesca Cavallo[a,b], and Sanjay Krishna[a,b,1]

[a]Department of Electrical and Computer Engineering, University of New Mexico, Albuquerque, NM 87106; [b]Center for High Technology Materials, University of New Mexico, Albuquerque, NM 87106; [c]Sandia National Laboratories, Albuquerque, NM 87123; [d]Raytheon, Albuquerque, NM 87106; [e]Laboratório Nacional de Nanotecnologia, Centro Nacional de Pesquisa em Energia e Materiais, 13083-100 Campinas, SP, Brazil; and [f]Departamento de Física, Universidade Federal de Viçosa, 36570-000 Viçosa, MG, Brazil

Edited by John A. Rogers, University of Illinois at Urbana–Champaign, Urbana, IL, and approved November 15, 2016 (received for review September 19, 2016)

Antimonide compounds are fabricated in membrane form to enable materials combinations that cannot be obtained by direct growth and to support strain fields that are not possible in the bulk. InAs/(InAs,Ga)Sb type II superlattices (T2SLs) with different in-plane geometries are transferred from a GaSb substrate to a variety of hosts, including Si, polydimethylsiloxane, and metal-coated substrates. Electron microscopy shows structural integrity of transferred membranes with thickness of 100 nm to 2.5 μm and lateral sizes from 24 × 24 μm^2 to 1 × 1 cm^2. Electron microscopy reveals the excellent quality of the membrane interface with the new host. The crystalline structure of the T2SL is not altered by the fabrication process, and a minimal elastic relaxation occurs during the release step, as demonstrated by X-ray diffraction and mechanical modeling. A method to locally strain-engineer antimonide-based membranes is theoretically illustrated. Continuum elasticity theory shows that up to ∼3.5% compressive strain can be induced in an InSb quantum well through external bending. Photoluminescence spectroscopy and characterization of an IR photodetector based on InAs/GaSb bonded to Si demonstrate the functionality of transferred membranes in the IR range.

antimonide | membranes | transfer | infrared | integration

Epitaxially grown Sb compounds have recently received increasing attention as functional layers in IR detectors (1–4) and sources (5–9), high-mobility transistors (10–12), resonant tunneling diodes (13–15), and low-power analog and digital electronics (10, 16). In this scenario we establish a versatile process to release and transfer Sb-based heterostructures from their epitaxial growth substrate to any host, resulting in fabrication of freestanding membranes (17, 18). Despite the numerous demonstrations of membrane technology applied to III-V semiconductors (18–26), fabrication and detailed characterization of Sb compounds in membrane form has not been reported. For the purpose of this work we investigate InAs/(Ga,InAs)Sb type II superlattices (T2SLs) and AlInSb/InSb quantum wells (QWs), but our approach is readily applicable to any Sb-containing heterostructure. We demonstrate that wet and dry techniques (17, 18) (i.e., transfer in liquid or mediated by a stamp, respectively) yield successful transfer of T2SL membranes with thickness ranging from 100 nm to 2.5 μm, and lateral sizes going from 24×24 μm^2 to 1×1 cm^2. We bond InAs/(InAs,Ga)Sb T2SLs to a large variety of hosts, including elastomers and rigid substrates, and both insulating and semiconducting substrates. Electron microscopy and X-ray diffraction (XRD) show that the crystal structure and the strain state of the materials are minimally altered during the release and transfer process. Mechanical modeling establishes that elastic strain up to ∼3.5% can be imparted in nanoscale-thickness AlInSb/InSb/AlInSb membranes by external bending. Finally, we demonstrate the functionality of Sb-based superlattices bonded to Si via photoluminescence (PL) and characterization of an IR detector fabricated on transferred InAs/InAsSb membranes.

Fabrication of Sb compounds in membrane form will significantly alter the landscape, as it relates to fundamental studies, properties, and applications of these materials. For instance, transfer of Sb compounds to insulating materials will enable the use of Hall and Van der Pauw measurements to investigate electrical transport in Sb-based T2SLs and QWs. Sb-based T2SLs bonded to Si will lead to fabrication of IR detectors with high signal-to-noise ratio, because Si is transparent to the incoming radiation, unlike the native GaSb substrate (27, 28). Transferring Sb-based membranes on a compliant host will pave the road to manufacturing of IR imagers and high-speed electronics in flexible form. An additional benefit of membrane technology applied to Sb-based membranes is the possibility to engineer strain distributions, which are not obtainable within the limitations of epitaxial growth processes (29, 30). Sb-based heterostructures may be bonded and conformed to patterned surfaces of various shapes and sizes to induce local strain of different types and amplitudes. Because strain significantly enhances both electron and hole mobilities in Sb-compounds, any electronic device will benefit from this type of strain engineering.

Significance

In this work we present a versatile method to fabricate antimonide-based heterostructures in membrane form, and we demonstrate the potential of these materials to enable hybrid integration and elastic strain engineering. The relevance of our work is threefold. First, integration of Sb-based compound membranes with Si substrates will potentially solve a number of technological challenges in the fabrication of IR optoelectronic devices based on type II superlattices. Second, transfer of Sb compounds to insulating materials will enable a thorough investigation of electrical transport in the heterostructure via Hall and Van der Pauw measurements. Third, membrane technology applied to Sb-based structures will enable one to engineer strain distributions, which are not obtainable within the limitations of epitaxial growth processes.

Author contributions: F.C. and S.K. designed research; M.Z., F.A., A.R., N.M.D., T.S.-S., and S.O.F. performed research; M.Z. and A.R. performed continuum mechanical modeling; B.A.K. and T.S.-S. performed material growth; N.M.D. performed atomic force microscopy; C.F.D. and S.O.F. performed X-ray diffraction measurements and data analysis; M.Z. and F.C. analyzed data; and M.Z., B.A.K., C.F.D., F.C., and S.K. wrote the paper.

The authors declare no conflict of interest.

This article is a PNAS Direct Submission.

Freely available online through the PNAS open access option.

[1]To whom correspondence may be addressed. Email: marziyeh.zamiri@gmail.com or skrishna@chtm.unm.edu.

This article contains supporting information online at www.pnas.org/lookup/suppl/doi:10.1073/pnas.1615645114/-/DCSupplemental.

Results and Discussion

Fabrication of Sb-based membranes begins with molecular beam epitaxy of InAs/(InAs,Ga)Sb T2SLs on a 60-nm $Al_{0.4}Ga_{0.6}Sb$ sacrificial layer. Composition and thickness of the AlGaSb film are carefully selected to avoid any plastic deformation during epitaxial growth. A detailed description of the as-grown layer structure is reported in the *SI Text, Epitaxial Growth*, along with the growth conditions. Next, we release as-grown membranes by selective removal of the $Al_{0.4}Ga_{0.6}Sb$ film in a diluted hydrofluoric acid (HF) solution (31). We use wet and dry transfer (17, 18) to a new host for membranes with 1×1 cm^2 and arrays of T2SLs with small lateral sizes ($\sim 24 \times 24$ μm^2). A detailed description of the transfer methods can be found in *Materials and Methods* as well as in *Supporting Information*.

We demonstrate transfer of T2SL membranes with different in-plane geometry, thickness, and layer structure. Fig. 1 *A–C* shows a schematic cross-sectional view and scanning electron micrographs (SEMs) of 100-nm-thick InAs/GaSb T2SLs after release and wet transfer to an Si substrate. Fig. 1*D* is an SEM of a partially released membrane, which is still coated with a photoresist protective layer. A 1.6-μm-thick membrane with identical layer structure is transferred to bulk Si using a Ti/Au coating as protective layer (see Fig. 1 *E–H*). Fig. 1*H* is a high-magnification SEM showing that a minimal lateral etching occurs at the membrane side walls.

We achieve release and dry transfer of 2.5-μm-thick InAs/InAsSb T2SL patterned in a 2D array of 24×24 μm^2 mesas or pixels. Fig. 1 *I* and *J* show a cross-sectional view of the transferred membrane and an SEM of pixels bonded to bulk Si, respectively. Fig. 1*K* is a high magnification and off-axis SEM of a single pixel. The transferred membrane exhibits smooth side walls (Fig. 1*L*), thereby confirming the excellent selectivity of the etching solution between InAs/InAsSb and the sacrificial layer (32).

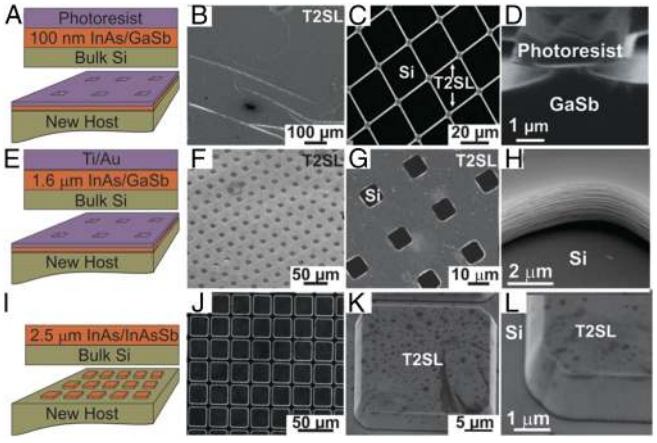

Fig. 1. Schematic cross-sectional views and SEM of transferred T2SL transferred to various substrates. Cross-section (*A*) and top-view SEM (*B* and *C*) of a 100-nm-thick InAs/GaSb T2SL with two different in-plane patterns transferred to a Si substrate. Photoresist serves as a protective coating during membrane release. (*D*) Off-axis SEM of a partially released 100-nm InAs/GaSb T2SL bonded to native growth substrate and coated with photoresist. Layer structure (*E*) and SEM images (*F* and *G*) of a 1.6-μm-thick InAs/GaSb SL membrane bonded to bulk Si. A Ti/Au film hinders etching of the active layer as removal of the sacrificial layer occurs. (*H*) Off-axis SEM of the membrane side wall, showing that a minimal lateral etching of the GaSb layer occurs during release of the InAs/GaSb SL membrane. (*I*) Schematic of a 2.5-μm-thick InAs/InAsSb T2SL after release and dry transfer to a Si substrate. (*J*) Top-view SEM of a 2D array of pixels on bulk Si. (*K*) Off-axis SEM of a single pixel. Dry transfer of the mesas is mediated by thermal release tape. Tape residues are visible on the surface of the pixel. (*L*) A high-magnification SEM of the smooth membrane side wall, showing that no lateral etching of the T2SL occurs during the release step.

Residual $Al_{0.4}Ga_{0.6}Sb$ may result in an increased roughness of the membrane backside, thereby promoting a weak bond between the membrane and the new substrate. Transfer of membranes on metal-coated substrates may also be used to provide the T2SL with electrical contacts via interface bonding (23, 33). In this scenario, a residual $Al_{0.4}Ga_{0.6}Sb$ will drastically increase the resistance of the contact.

To confirm that the selective etching step completely removes the sacrificial layer, we compare the surface topography of the top and bottom surface of the released membrane using atomic force microscopy (AFM) (*Supporting Information*). Furthermore, we perform scanning transmission electron microscopy (STEM) and energy dispersion X-ray spectroscopy (EDS) to investigate the chemical composition and the structural quality of a 2.5-μm-thick InAs/InAsSb T2SL bonded to Si. Before membrane transfer, Si is coated with a Ti/Au/Ti film. The T2SL is patterned in a 24×24 μm^2 pixel before release and dry transfer to the new host. Milling by a focused ion beam is used to obtain a thin lamella across the T2SL/Si interface (Fig. 2 *A* and *B*). Remarkably, Fig. 2 *A* and *B* rule out the presence of voids or particles at the membrane/host interface, by showing a continuous interface bond. Fig. 2*C* is an STEM image of the T2SL/substrate interface, where the material contrast allows identifying the multilayered structure of the SL and the metal-coated substrate. The yellow line marks the path of the EDS chemical analysis, and the arrow indicates the direction of the performed line scan. The concentration of Ga, Sb, In, As, O, Ti, Au, and Si are extracted from the energy dispersive spectra and displayed in Fig. 2*D*. The magnitudes of each elemental profile are normalized to the values obtained for Si. The intensity modulation of the STEM image allows accurate correlation with the EDS scans through the interface. In, As, and Sb show an oscillating profile over the T2SL. The Au signal correlates with the bright region in Fig. 2*C*, and the Ti has a bimodal peaking between the Au and the SL, and between the Au and the Si signal.

As demonstrated in Fig. 1, we have established a successful process to release and transfer T2SL membranes onto any host substrate. Because transfer occurs through release of the membrane into a fluid, there is no resistance to strain relaxation, and elastic strain transfers between the various layers in the SL (17, 30). Furthermore, global and local bending of the membrane typically occurs during release and transfer. Strain redistribution among the layers may affect the electronic structure of the SL (e.g., change the intraband energy gap) (34). In addition, strain induced by bending or wrinkling can dramatically reduce the critical thickness of each layer for dislocation formation (35, 36). All of these phenomena will significantly affect the performance of any devices embedding T2SLs or any Sb-containing heterostructure (37–39). Based on these considerations, as-grown and transferred membranes undergo coplanar (out-of-plane) and GI XRD to evaluate the effect of the release and transfer process on the crystalline quality and strain state of the membranes. Both InAs/GaSb and InAs/InAsSb membranes are investigated. Fig. 3*A* shows the out-of-plane XRD pattern acquired from the as-grown AlGaSb/InAs/GaSb/InSb multilayer stack on a GaSb substrate. Nominal thickness of the T2SL is 1.6 μm. A thin InSb is grown at the GaSb/InAs interfaces to achieve a strain-balanced heterostructure (40) (*Materials and Methods*). Experimental data are acquired around the GaSb (004). The pattern is dominated by the substrate peak at a Bragg angle of $24.005°$ and by the zeroth-order peak of the SL structure at $24.026°$. We identify SL fringes up to the fourth order, and a shoulder (at lower Bragg angles than the substrate peak) that we ascribe to the contribution of the $Al_{0.4}Ga_{0.6}Sb$ sacrificial layer. The sharp SL fringes as well as the relatively high intensity of the zeroth-order reflection compared with the substrate peak demonstrate the high epitaxial quality of the as-grown

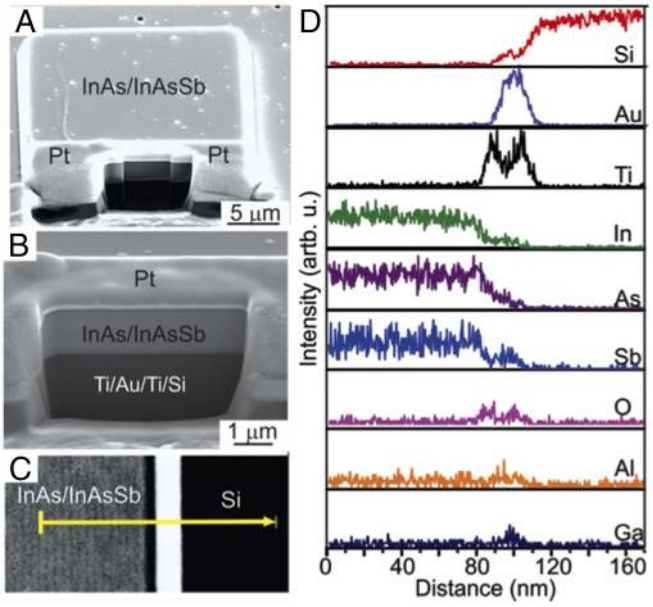

Fig. 2. Structural characterization of the bonded interface between a 2.5-μm-thick InAs/InAsSb SL and a metal-coated Si substrate. (*A* and *B*) Off-axis SEM image of an InAs/GaSb SL mesa transferred to a metal-coated Si substrate. The visible cross-section across the bonded interface is obtained by focused ion beam (FIB). Remarkably, *A* and *B* show a continuous bond between the membrane and the new host. (*C*) High-angle annular dark-field STEM across the bonded interface. The material contrast allows identifying the T2SL, as well as the Ti/Au bilayer deposited on Si before membrane transfer. (*D*) Elements concentration profiles obtained by EDS in the direction marked by the white arrow in *C*.

structure. Fig. 3*A*, *Inset* depicts the obtained GI-XRD reflection for the as-grown and the transferred T2SL. The two patterns correspond to two perpendicular (220) directions. We observe a single peak for the as-grown and transferred membranes, signifying that both structures are characterized by a single in-plane lattice parameter (i.e., they are pseudomorphic epitaxial layer stacks). The peaks acquired from the as-grown membrane are centered at the angle corresponding to the GaSb lattice parameter ($a_{GaSb,bulk}$ = 6.0959 Å). The two patterns acquired from the transferred sample exhibit both broadening and a shift to 33.428° indicating a relaxation of the lattice during the transfer. The calculated in-plane lattice parameter for the transferred membrane is 6.10177 ± 0.0052 Å (i.e., 0.096% bigger than the initial GaSb lattice parameter).

To deduce the various layer thicknesses for the as-grown multilayer, we fit the experimental data in Fig. 3*A* with a calculated pattern from a model structure. For this purpose, we use a generic optimization algorithm. The model assumes a pseudomorphic heterostructure to the GaSb substrate. We extract the following structural parameters for the as-grown multilayer: 50 nm $Al_{0.3}Ga_{0.7}Sb$/5 nm GaSb followed by a 312 period SL of 2.16 nm InAs/2.14 nm GaSb/0.26 nm InSb. The layer structure calculated from analysis of the coplanar XRD scans agrees with the one expected from the used growth conditions. The resulting fit demonstrates that the whole stack is pseudomorphic to the GaSb substrate. We observe additional satellite peaks in the experimental data that we ascribe to multidiffraction effects.

Fig. 3*B* shows the coplanar diffraction pattern of the transferred membrane (solid black circles). The pattern is dominated by the zeroth-order peak of the transferred structure now found at 24.019°. A careful inspection reveals a small systematic shift in the higher-order superlattice fringes compared with the diffraction pattern acquired from the as-grown sample (Fig. 3*A*). It is worth pointing out that the substrate peak and the typical shoulder of the AlGaSb layer have vanished because the membrane has been transferred to a new host substrate. Interestingly, we still observe the additional satellite peaks ascribed to multidiffraction effects of the T2SL suggesting that release and transfer does not degrade the crystalline quality of the film. We calculate the expected diffraction pattern for the transferred membrane (red curve) and compare it to the measured data. In this analysis we use the layer thickness obtained from fitting the coplanar scans of the as-grown samples as well as the in-plane lattice parameter deduced from the GI-XRD scans ($a_{in-plane} = 6.10177$ Å). Fig. 3*B* shows that such a fitting procedure produces a curve in good agreement with the experimental data. These results confirm both the structural model calculated from the coplanar scans of the as-grown multilayers and the in-plane lattice parameter obtained from the GI-XRD measurements.

We carry out a similar analysis for a 2.5-μm-thick InAsSb/InAs T2SL membrane. Fig. 3*C* shows the coplanar diffraction pattern (solid black circles) around the (004) GaSb peak of the as-grown AlGaSb/InAs/InAsSb multilayer. The pattern is dominated by the GaSb substrate and the zeroth-order superlattice peaks at 24.01° and 24.03°, respectively. We identify the typical shoulder arising from the AlGaSb sacrificial layer as well as several superlattice fringes at lower and higher angles than the main peaks of the diffraction pattern. The large number of observable superlattice fringes indicates a good pseudomorphic crystal structure of the as-grown multilayer stack. We perform GI-XRD around the in-plane (220) reflection of the as-grown and the transferred membranes. Data are acquired around two perpendicular directions for the as-grown sample and at one reflection for the transferred membrane, as shown in Fig. 3*C*, *Inset*. We find the substrate reflections close to their average position of 33.46° (i.e., in good agreement with the first sample set). We ascribe the broad features dominating the GI-XRD of the as-grown membrane to the large thickness of the superlattice, which may result in an inhomogeneous strain distribution. Interestingly, upon release, the (220) reflection sharpens, indicating a more equal distribution of strain inside the transferred membrane. Calculations of the in-plane lattice parameter of the transferred membrane from Bragg's law yield $a_{in-plane} = 6.1000 \pm 0.0074$ Å, which is 0.066%, larger than the lattice parameter of the as-grown structure.

Following procedure reported for the InAs/GaSb SL, we determine the layer structure (right inset in Fig. 3*C*) by fitting a calculated diffraction pattern to the coplanar scans. The deduced parameters are a 50-nm $Al_{0.3}Ga_{0.7}Sb$ layer followed by 340 periods of the 3-nm $InAs_{0.78}Sb_{0.22}$/4.4 nm InAs superlattice. Good agreement is found with what is expected from the growth conditions. Hereby, a single InAsSb layer represents the digital InAs/InSb alloy. We observe a set of reflections that cannot be fitted by partly relaxing the SL membrane but are compatible with a structure that would have double the thickness for the InAsSb and InAs layer. Therefore, we ascribe these reflections to multiple diffraction effects due to the large number of periods and large total thickness of the T2SL.

To confirm the strain relaxation of the transferred InAs/InAsSb SL membrane, we carry out coplanar diffraction around the (004) reflection of the membrane. The obtained pattern is depicted in Fig. 3*D*. We observe the zeroth-order SL peak shifted to 24.038°, along with SL fringes up to the fourth order. As expected, the GaSb substrate peak and the shoulder from the AlGaSb layer have vanished. We again identify several higher-orders SL fringes, but intensity between them reaches at some places the background level of our setup. Interestingly, the additional fringes observed for the as-grown sample are still present, indicating the excellent crystal quality of the transferred membrane. We relax the in-plane lattice parameter of the

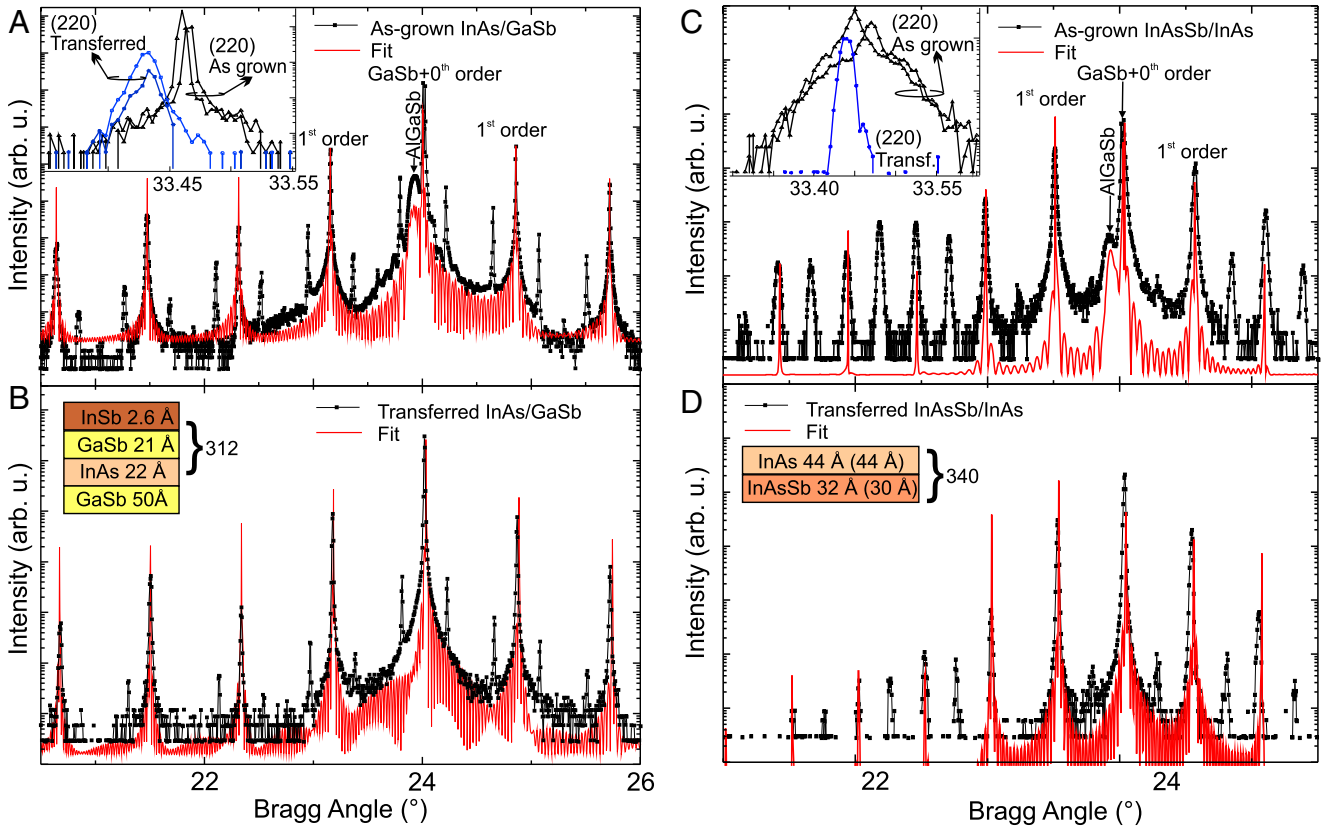

Fig. 3. (*A*) Coplanar diffraction pattern acquired around the (004) GaSb peak of the as-grown InAs/GaSb T2SL (solid black circles). A fit to the experimental data is plotted as a red line. (*Inset*) The pattern obtained by grazing-incidence (GI)-XRD around the (220) reflection of the as-grown (circle-line pattern) and the transferred sample (triangle-line pattern). (*B*) Coplanar XRD pattern acquired from a transferred InAs/GaSb SL on a Si substrate (solid black circles). (*Inset*) The layer structure obtained from the fit of the coplanar patterns, plotted as a red line. (*C* and *D*) Coplanar diffraction pattern of the as-grown (*C*) and transferred (*D*) InAs/InAsSb SL membrane (solid black circles). Both patterns are acquired around the GaSb (004) reflection. The inset in *C* shows theGI-XRD around two (220) reflections of the as-grown SL and one (220) reflection of the transferred multilayer stack. A fit to the experimental data is plotted as a red line in *C* and *D*. The model layer structure obtained from fitting the coplanar patterns is shown in *D*, *Inset*. A slight discrepancy in the layer thickness deduced from simulations of the data in *C* and *D* is observed. The thickness within brackets is obtained from fitting diffraction patterns of the as-grown membrane.

structural model deduced from the as-grown sample to the parameter determined from the GI-XRD ($a_{in-plane}$ = 6.100005 Å). Interestingly, we obtain a good agreement with the zeroth-order reflection, but the layer thickness requires a minimal change (see Fig. 3*D*, *Inset*: The thickness in the bracket is the thickness obtained from fitting diffraction patterns of the as-grown membrane).

Calculated values of in-plane strain in each layer of the SL are also reported along with the bulk lattice parameters per each constitutive material of the multilayer stack.

Finally, we evaluate the effect of the release and transfer process on the strain distribution in each layer of the T2SL. For this purpose, we calculate the in-plane strain in the as-grown and transferred membranes using the in-plane lattice parameters obtained from XRD (Table 1). Table 1 shows that the release and transfer process results in relaxation of the T2SL and redistribution of the strain established by epitaxial growth among the various layers in the SL. Specifically, while the membrane is freestanding in liquid, the strain through its thickness is balanced, such that only stretching occurs. During this process, part of the compressive strain established by epitaxial growth in the InSb layers transfers to InAs and GaSb, within the InAs/GaSb SL (30, 41). Similarly the Ga-free membrane elastically relaxes during transfer, resulting in the tensile strain in InAs to increase and in the InAsSb to become less compressive.

We compare the in-plane strain obtained for the transferred membrane via XRD and continuum mechanical modeling of an elastically multilayer (30, 41). In this analysis we assume that the strain state and the thickness of each layer within the SL are uniform in the growth direction. Furthermore, all of the layers are regarded as perfectly bonded at any stage of the process. We calculate the in-plane strain in the various layers of the InAs/GaSb T2SL using the equations below:

$$\varepsilon_{\mathrm{GaSb}} = \frac{\Sigma_1\eta_1\varepsilon_{m,1} - \Sigma_2\eta_2\varepsilon_{m,2}}{1 + \Sigma_1\eta_1 + \Sigma_2\eta_2} \quad [1]$$

$$\varepsilon_{\mathrm{InAs}} = -\frac{\varepsilon_{m,1}(1 + \Sigma_2\eta_2) + \Sigma_2\eta_2\varepsilon_{m,2}}{1 + \Sigma_1\eta_1 + \Sigma_2\eta_2} \quad [2]$$

$$\varepsilon_{\mathrm{InSb}} = \frac{\Sigma_1\eta_1\varepsilon_{m,1} + \varepsilon_{m,2}(1 + \Sigma_1\eta_1)}{1 + \Sigma_1\eta_1 + \Sigma_2\eta_2}, \quad [3]$$

where $\varepsilon_{m,1} = \varepsilon_{\mathrm{GaSb}} - \varepsilon_{\mathrm{InAs}}$ and $\varepsilon_{m,2} = \varepsilon_{\mathrm{InSb}} - \varepsilon_{\mathrm{GaSb}}$ are the mismatch strains between adjacent layers and $\Sigma_1 = M_{\mathrm{InAs}}/M_{\mathrm{GaSb}}$, $\Sigma_2 = M_{\mathrm{InSb}}/M_{\mathrm{GaSb}}$, $\eta_1 = t_{\mathrm{InAs}}/t_{\mathrm{GaSb}}$ and $\eta_2 = M_{\mathrm{InSb}}/M_{\mathrm{GaSb}}$ with M the biaxial modulus of the material and t layer thickness (30, 41).

Mismatch strain, $\varepsilon_{\mathrm{m,XRD}}$, between adjacent layers in the as-grown T2SLs, as deduced from XRD. Biaxial modulus, M = E/1 $-\nu$, with E, Young's modulus and ν the Poisson's ratio of the

Table 1. In-plane lattice parameters deduced from GI-XRD and coplanar XRD for the InAs/GaSb and InA/InAsSb T2SL both before and after transfer to bulk Si

			$a_{in\text{-}plane}$		$\varepsilon_{in\text{-}plane}$	
T2SL	Layer	a_{bulk}, Å	As-grown, Å	Transferred, Å	As-grown, %	Transferred, %
GaSb/InAs/InSb	GaSb	6.0959	6.0959	6.1017	0	0.095
	InAs	6.0583			0.62	0.072
	InSb	6.4790			−5.92	5.8
InAs/InAsSb	InAs	6.0583	6.0959	6.1000	0.62	0.69
	InAsSb	6.1424			−0.75	−0.69

materials (42). Residual in-plan strain as deduced from XRD, $\varepsilon_{in\text{-}plane,XRD}$, and from continuum mechanics modeling, $\varepsilon_{in\text{-}plane,CM}$.

We obtain Eqs. **1–3** using force balance between all of the layers in SL and the constraint of coherent lattice across the interfaces (41). A similar analysis yields Eqs. **4** and **5** to estimate in-plane strain in the InAs/InAsSb SL:

$$\varepsilon_{InAsSb} = \frac{1}{1+\Sigma_1\eta_1} \quad [4]$$

$$\varepsilon_{InAs} = \frac{1-\varepsilon_m(1+\Sigma_1\eta_1)}{1+\Sigma_1\eta_1}, \quad [5]$$

where $\varepsilon_m = \varepsilon_{InAsSb} - \varepsilon_{InAs}$ is the mismatch strain between InAsSb and InAs, $\Sigma_1 = M_{InAs}/M_{InAsSb}$ and $\eta_1 = t_{InAs}/t_{InAsSb}$. Biaxial modulus and layer thickness are indicated with M and t, respectively. In our analysis we use the layer thickness estimated from the coplanar XRD patterns of the as-grown membranes (Fig. 3 *B* and *D*), and we calculate the mismatch strain from the values obtained for the as-grown membrane from XRD (Table 1). Table 2 shows that the in-plane strain values obtained from XRD and those calculated using continuum mechanical models differ by 0.03–0.17%. We attribute this discrepancy to nonuniformity of the strain state and thickness of the various layers in the growth direction.

Antimonide-based membranes can be bonded to any material, including flexible and patterned substrate. Membranes bonded to flexible hosts may be stretched or bent to induce a uniform elastic strain in the film. Alternatively, freestanding membranes can be transferred and conform to micro- and nano-scale patterned features due to their extremely low bending stiffness (43). In this case the film undergoes local elastic deformation (i.e., bending). Global or local bending (44, 45) may be used to impart a controlled amount of elastic strain in Sb compounds. We demonstrate the potential of membrane technology to strain-engineer (17, 30) Sb-based compounds, thereby enhancing electrical transport in these materials. For this purpose we use continuum mechanical modeling to estimate the amount of strain imparted through bending in a 10-nm InSb membrane cladded by 30-nm $Al_{0.2}In_{0.8}Sb$. InSb QWs exhibit a relatively high hole mobility because the structure is under significant biaxial compressive strain due to the lattice mismatch between InSb and $Al_xIn_{1-x}Sb$ (46). Transfer of a thin InSb/$Al_xIn_{1-x}Sb$ heterostructures to a textured surface with an array of micro/nanospheres allows increasing the amount of strain in InSb beyond the limitations of epitaxial growth. Fig. 4 *A–C* schematically illustrate membrane transfer to a textured substrate. Initially the membrane is bonded to its native substrate (Fig. 4*A*), and it is pseudomorphically strained to the lattice parameter of the substrate. During release the membrane is freestanding, and hence free to elastically relax. Wet transfer (Fig. 4*B*) to a textured surface results in the membrane's experiencing spherical bending and biaxial strain (Fig. 4*C*). Micro/nanospheres on a substrate can be obtained by a variety of processes, including self-assembly of silica spheres and templating by colloidal crystals (47, 48). We calculate the strain distribution across the thickness of a 30/10/30-nm $Al_{0.2}In_{0.8}Sb$/InSb/$Al_{0.2}In_{0.8}Sb$ under a spherical bending of radius R = 5 μm. Heterostructures are modeled as-grown on $Al_{0.2}In_{0.8}Sb$ relaxed buffers. Sketches of the bent membrane and the calculated in-plane strains are in Fig. 4 *D* and *E*, respectively. The strains in the as-grown and freestanding membranes are also plotted in Fig. 4*E*. As-grown InSb experiences a 1.06% biaxial compressive strain, whereas no deformation occurs in the $Al_{0.2}In_{0.8}Sb$ layer upon growth (green lines in Fig. 4*E*). During release the membrane undergoes elastic relaxation yielding a 0.9848% compressive strain in InSb and a 0.0752% tensile strain in $Al_{0.2}In_{0.8}Sb$ (red lines in Fig. 4*E*). Strain values in the released membranes are calculated as described in *Supporting Information*. A spherical bending with a radius of curvature R = 5 μm produces a linearly varying strain across the heterostructures ranging from ∼−1.9 to ∼−2.1%, which includes the strain due to the release process. Fig. 4*F* plots the average, minimum, and maximum volumetric strain in InSb for R going from 0.1 to 5μm. Minimum and maximum strains are calculated at the two InSb/$Al_{0.2}In_{0.8}Sb$ interfaces. Average values of compressive strain remain more or less constant at ∼2% for R ∼0.3 – 5μm. A higher strain gradient at low R results in the volumetric strain to increase up to ∼3.8% at $R = 0.1\mu m$.

T2SL membranes hold a tremendous potential as absorbers in wafer-level IR detectors. The high cost of present-day photonic focal plane arrays results from low-yield, die-level fabrication steps, such as flip-chip bonding to an Si read-out integrated circuit, underfill epoxy, and substrate removal. Integration of Sb-based SL membranes with Si substrates could open up a new paradigm to develop IR detectors. We demonstrate the technological value of antimonide-based membranes for IR applications via PL spectroscopy and characterization of a

Table 2. Layer thickness within the InAs/GaSb and the InAs/InAsSb SL as expected from the epitaxial growth conditions

T2SL	Layer	Thickness, nm	$\varepsilon_{m,XRD}$, %	M, GPa	$\varepsilon_{in\text{-}plane,XRD}$, %	$\varepsilon_{in\text{-}plane,CM}$, %
GaSb/InAs/InSb	InAs	2.2	−0.62	791	0.72	0.55
	GaSb	2.1		914	0.09	0.07
	InSb	0.26	6.52	629	−5.80	−5.98
InAs/InAsSb	InAs	4.4	−1.37	791	0.69	−0.59
	InAsSb	3.2		760	−0.69	−0.72

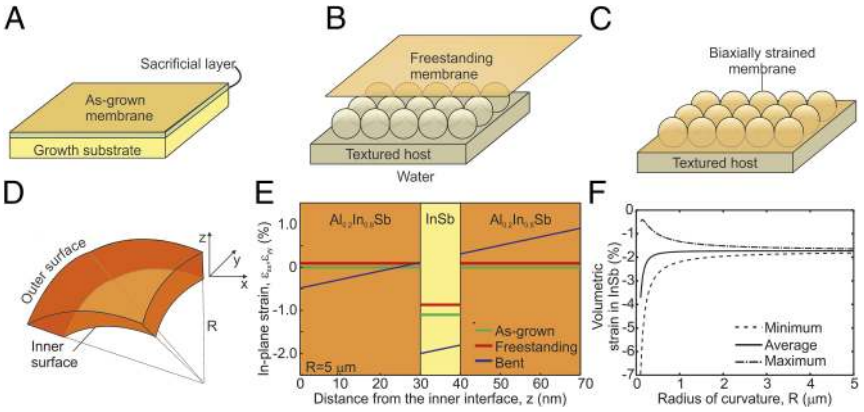

Fig. 4. Strain engineering of Sb-based heterostructures. (*A*–*C*) Schematic illustration of membrane transfer to a substrate textured with a 2D array of spheres. (*A*) As-grown membranes bonded to their sacrificial layer are pseudomorphically strained to the native substrate. Wet transfer of membranes (*B*) to a textured host results in the film's conforming to the shape of the pattern. Strain redistributes across layers because the membrane is freestanding in liquid. (*C*) Biaxially strained membrane. The textured host in *B* and *C* can be obtained through a variety of processes, including self-assembly of silica spheres and templating by colloidal crystals. (*D*) Section of a membrane undergoing spherical bending with a radius of curvature R. (*E*) In-plane strain profile across the thickness of an AlInSb/InSb/AlInSb heterostructures. Strain in the as-grown (green), freestanding (red), and spherically bent (black) membranes is plotted. (*F*) Minimum, maximum, and average strain in the InSb QW vs. a radius curvature varying between 0.1 and 5 μm.

photodetector based on an InAs/GaSb T2SL bonded to Si. Fig. 5*A* compares the normalized PL spectra acquired at 77 K from an InAs/GaSb T2SL supported by the growth substrate, and after release and transfer to bulk Si. The 1.6-μm-thick membranes are patterned in a 2D array of 24×24 μm^2 mesas while on the native substrate. Both the as-grown and transferred T2SLs exhibit a narrow PL spectrum centered at 3.85 μm (0.3220 eV) (Fig. 5*A*). We attribute the single peak in the PL spectra to the electronic transition between first subband in the conduction band (C1) and the first heavy hole subband in the valence band (HH1). To verify our hypothesis we calculate the band structure of the as-grown and transferred InAs/GaSb T2SL using the empirical pseudopotential method (49, 50) (*Supporting Information*). Theoretical modeling relies on layer thickness and in-plane lattice parameters estimated by XRD (Table 1). The empirical pseudopotential method yields C1–HH1 transition energies of 0.2920 eV (corresponding to 4.246 μm) and 0.2933 eV (corresponding to 4.227 μm), for the as-grown and transferred membranes, respectively. Theoretical predictions confirm the origin of the single PL peak shown in Fig. 5*A*. The discrepancy between the transition energies obtained experimentally and estimated through the empirical pseudopotential method have been previously reported and attributed to chemical nonabruptness of the interfaces (51). Remarkably, modeling shows that alteration of the in-plane lattice parameter of the T2SL, as estimated by XRD, yields a minimal increase (i.e., 1.3 meV) of the C1–HH1 transition energy. A corresponding blue shift of 18 nm is expected in the PL peak acquired from the transferred membrane, with respect to the spectrum of the as-grown multilayer. The estimated changes in the spectra are below the resolution of the measurement setup.

A decrease by 75% of the absolute PL intensity is observed after membrane transfer (see nonnormalized PL spectra reported in *SI Text, PL at 77K*). We attribute this change in the absolute PL intensity to the reduced volume of the emission in the transferred membrane. Indeed, only 75% of the fabricated pixels are successfully bonded to the new host. In addition, roughening of the membrane side walls during release (Fig. 5*A*) may enhance nonradiative recombination (52, 53).

Finally, we fabricate a proof-of-concept photodetector based on a 1.6-μm-thick InAs/GaSb p-i-n SL bonded to bulk Si. For this purpose, we dry-transfer a 24×24μm^2 membrane to a Si substrate coated with a Ti (50 Å)/Au (150 Å)/Ti (50 Å) film, which serves as the bottom contact of the detector. Following process steps are passivation of the device side walls by Si_3N_4 and definition of the top and bottom contact geometries (*Materials and Methods*). Fig. 5*b*, *Inset* is a top-view optical image of the photodetector. We compare spectral response and dark current

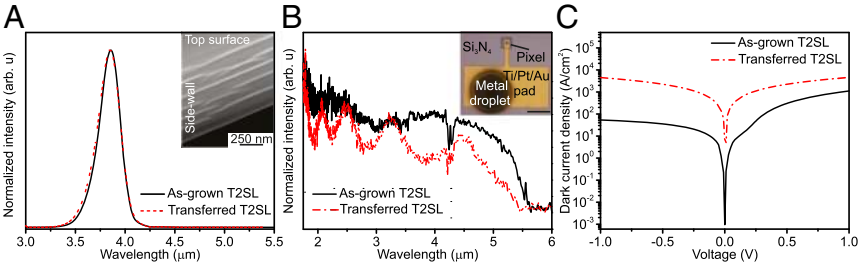

Fig. 5. Functional characterization of 1.6-μm-thick InAs/GaSb T2SLs at 77 K. The lateral dimension of the membrane is 24×24μm^2. (*A*) Normalized PL spectra acquired from the as-grown and transferred InAs/GaSb T2SLs. The spectral features are dominated by a single peak centered at 3.85μm. (*Inset*) Off-axis SEM illustrating rough side walls of the membrane after transfer to bulk Si. (*B*) Spectral response of InAs/GaSb photodetectors fabricated on as-grown (solid black line) and transferred (red dash-dotted line) T2SLs. (*Inset*) Top-view optical image of the device based on the transferred membrane to metal-coated Si. The top contact pads as well as residues of a bonded wire are also visible. (Scale bar, 50 μm.) (*C*) Current density-voltage characteristic acquired from detectors under no illumination. The solid black line and the red dash-dotted line correspond to the device fabricated on the as-grown and transferred membranes, respectively.

density of devices based on T2SLs on their growth substrates and on bulk Si. Both devices embed 24 × 24 μm^2 IR absorbers. We perform device characterization at 77 K (i.e., the typical operating temperature of IR detectors). Fig. 5*B* shows that both fabricated devices exhibit a spectral response covering a 1.7 to 5.7 μm wavelength range. The visible oscillations in the spectral response of the photodetector based on the transferred membrane originate from multiple reflections at the metal-coated Si surface (54). Fig. 5*C* compares the dark current densities of the two fabricated devices between −1 V and 1 V. We measure a typical p-i-n current density-voltage (J-V) characteristic for a detector with a small perimeter-to-area ratio fabricated on the as-grown T2SL. However, the dark current density (J) of the device manufactured on the transferred membrane is symmetrical about the zero voltage axis. Furthermore, the dark current density of the device on bulk Si is 4 × 10^4 A/cm^2, which is two orders of magnitude lower compared with values measured for the device on the native substrate. Both highlighted features of the J-V characteristics measured for the detector on Si suggest that the current follows a low resistance path along the device side walls (55). We attribute the higher conductance of the membrane perimeter to the poor selectivity of the etching solution with respect to GaSb and resulting lateral etching of material during the release process (Fig. 5*A*, *Inset*) (32). We envision that detector performance can be enhanced by protecting the top as well as the side walls of the T2SL during the release process (56, 57).

Conclusions

We have demonstrated fabrication, heterogeneous integration, and strain-engineering of Sb-based membranes. Our approach is based on selective etching of an $Al_{0.4}Ga_{0.6}Sb$ sacrificial layer followed by wet or dry transfer processes. We have successfully bonded Sb-based membranes with thickness in a 0.1- to 2.5-μm range, as well as patterned in a variety of lateral geometries. Remarkably, the crystalline quality, chemical composition, and strain state of the T2SLs are not significantly affected by the release and transfer process, as demonstrated by a detailed materials characterization. Inspired by nanomembrane technology, we established a technique that does not rely on direct growth to integrate Sb compounds with other materials. For the purpose of this work we have demonstrated integration of Sb-based membranes on bulk Si, as it is relevant to fabrication of focal plane arrays for IR imaging. However, our process is easily extendable to other substrates, such as insulators, flexible substrates, or patterned hosts. Therefore, a large variety of materials combinations comprising Sb-based SLs will be available through our approach. The field of IR imaging will particularly benefit from a high-yield and low-cost process to integrate T2SL on Si ROICs. In addition, Sb-based membranes on insulator substrates, such as SiO_2, may be used to investigate electrical transport in T2SLs or QWs, without the complication of a semiconducting substrate. Finally, we theoretically demonstrate that high-enough values of elastic strain to enhance carrier transport may be imparted to Sb compounds by release and conformal bonding to a patterned host. This type of strain engineering will enable tuning material properties and postepitaxial growth without varying the layer structure within the membrane.

Materials and Methods

Wet and Dry Transfer Process. We accomplish wet transfer of InAs/GaSb SLs to a new host by using a patterned photoresist or a Ti/Au film as protective layer of the membrane surface. Etching holes were defined by photolithography and a BCl_3 inductively coupled plasma (ICP) etching, through the epitaxial layer structure and down into the substrate. We intentionally overetched the samples all the way into the GaSb substrate, so that the $Al_{0.4}Ga_{0.6}Sb$ film is exposed to the etching solution. Releasing the membrane from the GaSb substrate was accomplished by selective etching of the $Al_{0.4}Ga_{0.6}Sb$ sacrificial layer in a diluted HF solution ([(HF:H_2O) 1:700]:ethanol 1:5) (31). Membrane release occurred in 6 h and 16 h for samples coated with Ti/Au and photoresist, respectively. A faster membrane release in presence of metal results from the Ti/Au's acting as a catalyst of the selective etching process (58). After complete removal of the AlGaSb the T2SL bonded back to the GaSb substrate. The sample was then transferred in deionized (DI) water, where the membrane floated off the support and became freestanding. The new host (or target substrate) was dipped into the DI water, and the membrane adhered to it through capillary action. Target substrates were cleaned with acetone and isopropanol and exposed to oxygen plasma.

In dry transfer, InAs/InAsSb T2SLs were patterned in a 2D array of 24 × 24μm^2 mesas. Spacing between the mesas was 6 μm both in the *x* and *y* directions. Patterning was performed by photolithography and ICP etching in BCl_3. The final etch depth was 2.6 μm, that is, higher than the epilayer thickness, thereby allowing complete access of the etching solution to the sacrificial layer. The $Al_{0.4}Ga_{0.6}Sb$ sacrificial layer was partially etched in diluted HF and ethanol solution ([(HF:H_2O) 1:700]:ethanol 1:5). After 4.5 h, the sample was rinsed in DI water and dried with nitrogen. Partially released membranes were removed from the native growth substrate using either a polydimethylsiloxane (PDMS) stamp or thermal release tape (Semiconductor Equipment Corp.). The PDMS was prepared using a Sylgard 184 kit, using a previously reported procedure (18). Dry transfer to the new host was accomplished by a printing process. Release of PDMS stamps and thermal release tapes have been previously described (18, 42). The target substrate was cleaned as described for the wet transfer.

EM and EDS. SEM images were taken by a JEOL 5800LV system in high-vacuum mode using a secondary electrons detector. A cross-section of the InAs/InAsSb T2SL/bulk Si was prepared in a FEI Q3D ESEM/FIB dual-beam system with Ga ions source. TEM characterization was performed in a JEOL 2010F high-resolution TEM/scanning-TEM with field emission e-beam accelerated at 200 kV. Chemical analysis via EDS was accomplished on the JEOL 2010F in STEM mode. The measurement was performed using the X-MaxN 80T, 80-mm^2 detector (Oxford Instruments) with a resolution 50,000 cps at 200 kV. Aztec software provides the power to acquire and process the EDS data.

PL Spectroscopy. PL spectroscopy was conducted using a 1.5-W argon laser as excitation source. The emitted PL was collected using CaF_2 lenses and Al mirrors and focused into a monochromator with a grating optimized for a 2.6- to 6-μm wavelength range. The PL intensity was measured through an InSb detector (5.5-μm cutoff wavelength), positioned at the output of the monochromator. A chopper was used to modulate the optical excitation on the sample and a lock-in amplifier was used for the detection.

XRD. Coplanar and GI-XRD measurements were carried out at the XDR2 beamline of the Brazilian Synchrotron Light Facility (LNLS) using a beam energy of 10 keV (wavelength $\lambda = 1.24093$ Å) with a six-circle diffractometer. The size of the X-ray beam is 0.3 × 4.0 mm^2 for all of the out-of-plane measurements. For the GI-XRD, the all-sample surface is captured during the measurement as a result of the shallow incident angle. Sb-based SLs were investigated by XRD before and after transfer to a new host, namely Si. Coplanar measurements were performed around the GaSb (004) reflection. GI-XRD measurements were performed with an incident angle of 0.2° at the (220) reflection. Diffraction patterns of the coplanar measurements were fitted by a commercial software package, resulting in a structure based on the initial growth recipe.

Device Fabrication. InAs/GaSb pixels were first transferred onto a supporting Si substrate coated with a Ti (50 Å)/Au (150 Å)/Ti (50 Å) film. The metal layers served as the bottom contact of the detectors. The transferred membranes were annealed at 150 °C on a hot plate for 5 min. Any native oxide film grown on the side walls of the mesas was removed by a 30-s etching in hydrochloric solution (HCl:DI water/1:20). Then, 100 nm of Si_3N_4 was deposited by plasma-enhanced chemical vapor deposition as a blanket coating, covering all of the pixels and substrate. This dielectric layer passivated the photodetector pixels and promoted adhesion of the pixels to their new substrate. The dielectric layer also acted as an insulator between the top and bottom contacts. Next, a lithography step was undertaken and a dry reactive ion etch was performed to open areas in the Si_3N_4 for metallization. After standard photolithography to defined the top and bottom contacts,

native oxides were removed from the pixels, using diluted HCl:H_2O (1:20). Finally, ohmic contacts were thermally evaporated on the defined area using Ti (500 Å)/Pt (500 Å)/Au (3,000 Å).

Device Characterization. The current-voltage characteristic of the photodetector was measured at 77 K by a JANIS ST-500 micromanipulated probe station. The sample was placed in a 10^{-5} Torr vacuum during electrical characterization. The probe station was equipped with a Scientific Instruments M9700 temperature controller, and the measurements are carried out with a Keithley 2400 source measure unit.

To acquire the spectral response of the IR detector the light frequency of a broad-spectrum IR light source (Hawk Eye IR-18) was modulated by a chopper and sent through a monochromator with an optimized grating for a 3- to 9-μm wavelength range. A JANIS JPF-100 cryostat was used to cool the detector to 77 K. The device is biased by a preamplifier with 10^3 gain and 0.01 V bias. A lock-in amplifier was used to measure the resulting electric response of the device.

ACKNOWLEDGMENTS. We thank Sharon Steely for her help editing the paper and Dr. Ying-Bin Yang for his assistance in sample preparation via focused ion beam, electron microscopy, and electron dispersion spectroscopy. M.Z. thanks Vinita Dahiya and Dr. Alireza Kazemi for useful discussions. C.F.D. and S.O.F. acknowledge CNPq and LNLS for partially funding their work at the XRD2 beamline, and thank the beamline staff for their help and Sergio Luiz Morelhão for his comments during data analysis. C.F.D. thanks Fundação de Amparo à Pesquisa do Estado de São Paulo (FAPESP) for financial support. This work was supported by Air Force Research Laboratory Grant FA9453-14-1-0248 and the University of New Mexico Microelectronics Endowed Chair.

1. Rogalski A (2008) New material systems for third generation infrared photodetectors. *Opto-Electronics Rev* 16(4):458–482.
2. Kim HS, et al. (2008) Mid-IR focal plane array based on type-II InAs/GaSb strain layer superlattice detector with nBn design. *Appl Phys Lett* 92(18):183502.
3. Wei Y, Gin A, Razeghi M, Brown GJ (2002) Advanced InAs/GaSb superlattice photovoltaic detectors for very long wavelength infrared applications. *Appl Phys Lett* 80(18):3262–3264.
4. Kim HS, et al. (2012) Long-wave infrared nBn photodetectors based on InAs/InAsSb type-II superlattices. *Appl Phys Lett* 101(16):161114.
5. Bauer A, et al. (2009) Emission wavelength tuning of interband cascade lasers in the 3–4 μm spectral range. *Appl Phys Lett* 95(25):251103.
6. Bewley WW, et al. (2008) Gain, loss, and internal efficiency in interband cascade lasers emitting at λ = 3.6–4.1 μm. *J Appl Phys* 103(1):013114.
7. Hill CJ, Yang RQ (2005) MBE growth optimization of Sb-based interband cascade lasers. *J Cryst Growth* 278(1–4):167–172.
8. Shanabrook BV, et al. (1999) Engineered heterostructures of 6.1-angstrom III-V semiconductors for advanced electronic and optoelectronic applications. *SPIE's International Symposium on Optical Science, Engineering, and Instrumentation* (International Society for Optics and Photonics, Bellingham, WA), pp 13–22.
9. Sorokina IT, Vodopyanov KL (2003) *Solid-State Mid-Infrared Laser Sources* (Springer, New York), Vol 89.
10. Bennett BR, Magno R, Boos JB, Kruppa W, Ancona MG (2005) Antimonide-based compound semiconductors for electronic devices: A review. *Solid State Electron* 49(12):1875–1895.
11. Bennett BR, Chick TF, Ancona MG, Boos JB (2013) Enhanced hole mobility and density in GaSb quantum wells. *Solid State Electron* 79:274–280.
12. Wu B (2003) Sb-based high electron mobility transistors: Processing and device characterization. PhD thesis (Univ of Notre Dame, Notre Dame, IN).
13. Sun JP, Haddad GI, Mazumder P, Schulman JN (1998) Resonant tunneling diodes: Models and properties. *Proc IEEE* 86(4):641–660.
14. Akkala AG (2011) NEGF simulation of electron transport in resonant tunneling and resonant interband tunneling diodes. PhD thesis (Purdue Univ, West Lafayette, IN).
15. Manasreh MO (1997) *Antimonide-Related Strained-Layer Heterostructures* (CRC, Boca Raton, FL), Vol 3.
16. Bennett BR, Boos JB (2013) Antimonide-based compound semiconductors for low-power electronics (Naval Research Laboratory, Washington, DC).
17. Cavallo F, Lagally MG (2012) Semiconductor nanomembranes: A platform for new properties via strain engineering. *Nanoscale Res Lett* 7(1):1–10.
18. Takei K, et al. (2012) Nanoscale InGaSb heterostructure membranes on Si substrates for high hole mobility transistors. *Nano Lett* 12(4):2060–2066.
19. Ko H, et al. (2010) Ultrathin compound semiconductor on insulator layers for high-performance nanoscale transistors. *Nature* 468(7321):286–289.
20. Yablonovitch E, Gmitter T, Harbison JP, Bhat R (1987) Extreme selectivity in the lift-off of epitaxial GaAs films. *Appl Phys Lett* 51(26):2222–2224.
21. Owen DL, Lackner D, Pitts OJ, Watkins SP, Mooney PM (2009) In-place bonding of GaAs/InGaAs/GaAs heterostructures to GaAs (0 0 1). *Semicond Sci Tech* 24(3): 035011.
22. Renteria E, Addamane S, Shima D, Hains C, Balakrishnan G (2015) 3 μm thick GaSb membrane diodes integrated with CVD diamond heat spreaders for thermally managed TPV cells. *2015 IEEE 42nd Photovoltaic Specialist Conference (PVSC)* (IEEE, New York), pp 1–3.
23. Yang W, et al. (2010) Large-area InP-based crystalline nanomembrane flexible photodetectors. *Appl Phys Lett* 96:121107.
24. Yamaguchi H, Dreyfus R, Miyashita S, Hirayama Y (2002) Application of InAs free-standing membranes to electromechanical systems. *Jpn J Appl Phys* 41(4S):2519.
25. Mei Y, et al. (2007) Optical properties of a wrinkled nanomembrane with embedded quantum well. *Nano Lett* 7(6):1676–1679.
26. Malachias A, et al. (2008) Wrinkled-up nanochannel networks: Long-range ordering, scalability, and X-ray investigation. *ACS Nano* 2(8):1715–1721.
27. Delaunay PY, Nguyen BM, Hoffman D, Huang EKW, Razeghi M (2009) Background limited performance of long wavelength infrared focal plane arrays fabricated from M-structure InAs–GaSb superlattices. *IEEE J Quant Electron* 45(2):157–162.
28. Rhiger DR, et al. (2007) Progress with type-II superlattice IR detector arrays. *Defense and Security Symposium* (International Society for Optics and Photonics, Bellingham, WA), pp 654202–654202.
29. Paskiewicz DM, Savage DE, Holt MV, Evans PG, Lagally MG (2014) Nanomembrane-based materials for group IV semiconductor quantum electronics. *Sci Rep* 4:4218.
30. Paskiewicz DM, Tanto B, Savage DE, Lagally MG (2011) Defect-free single-crystal SiGe: a new material from nanomembrane strain engineering. *ACS Nano* 5(7):5814–5822.
31. Morpurgo AF, Van Wees BJ, Klapwijk TM, Borghs G (1997) Submicron processing of InAs based quantum wells: A new, highly selective wet etchant for AlSb. *Appl Phys Lett* 70(11):1435–1437.
32. Clawson AR (2001) Guide to references on III–V semiconductor chemical etching. *Mater Sci Eng R Rep* 31(1):1–438.
33. Zamiri M, et al. (2016) Indium-bump-free antimonide superlattice membrane detectors on silicon substrates. *Appl Phys Lett* 108(9):091110.
34. Qiao PF, Mou S, Chuang SL (2012) Electronic band structures and optical properties of type-II superlattice photodetectors with interfacial effect. *Opt Express* 20(3):2319–2334.
35. Euaruksakul C, et al. (2013) Heteroepitaxial growth on thin sheets and bulk material: Exploring differences in strain relaxation via low-energy electron microscopy. *J Phys Appl Phys* 47(2):025305.
36. Huang M, et al. (2009) Mechano-electronic superlattices in silicon nanoribbons. *ACS Nano* 3(3):721–727.
37. Steffens S, et al. (2014) Impact of dislocations and dangling bond defects on the electrical performance of crystalline silicon thin films. *Appl Phys Lett* 105(2): 022108.
38. Karpov SY, Makarov YN (2002) Dislocation effect on light emission efficiency in gallium nitride. *Appl Phys Lett* 81(25):4721–4723.
39. Ni K, et al. (2016) Electrical effects of a single extended defect in MOSFETs. *IEEE Trans Electron Dev* 63(8):3069–3075.
40. Song Y, et al. (2013) Growth optimization, strain compensation and structure design of InAs/GaSb type-II superlattices for mid-infrared imaging. *Chem Materials Sci* 2(2):46–56.
41. Roberts MM, et al. (2006) Elastically relaxed free-standing strained-silicon nanomembranes. *Nat Mater* 5(5):388–393.
42. Chen PC, et al. (2009) High-performance single-crystalline arsenic-doped indium oxide nanowires for transparent thin-film transistors and active matrix organic light-emitting diode displays. *ACS Nano* 3(11):3383–3390.
43. Cavallo F, Grierson DS, Turner KT, Lagally MG (2011) "Soft Si": Effective stiffness of supported crystalline nanomembranes. *ACS Nano* 5(7):5400–5407.
44. Malachias A, et al. (2009) Direct strain and elastic energy evaluation in rolled-up semiconductor tubes by x-ray microdiffraction. *Phys Rev B* 79(3):035301.
45. Songmuang R, Jin-Phillipp NY, Mendach S, Schmidt OG (2006) Single rolled-up SiGe/Si microtubes: Structure and thermal stability. *Appl Phys Lett* 88(2):021913.
46. Orr JMS, et al. (2007) A surface-gated InSb quantum well single electron transistor. *New J Phys* 9(8):261.
47. Zhang G, Wang D, Möhwald H (2005) Patterning microsphere surfaces by templating colloidal crystals. *Nano Lett* 5(1):143–146.
48. Zhang K, Wu W, Meng H, Guo K, Chen J-F (2009) Pickering emulsion polymerization: preparation of polystyrene/nano-SiO_2 composite microspheres with core-shell structure. *Powder Tech* 190(3):393–400.
49. Dente GC, Tilton ML (1999) Pseudopotential methods for superlattices: Applications to mid-infrared semiconductor lasers. *J Appl Phys* 86(3):1420–1429.
50. Schuler-Sandy T, et al. (2012) Gallium free type II $InAs/InAs_xSb_{1-x}$ superlattice photodetectors. *Appl Phys Lett* 101(7):071111.
51. Pavesi L, Guzzi M (1994) Photoluminescence of $AL_xGa_{1-x}As$ alloys. *J Appl Phys* 75(10):4779–4842.
52. Moser P (2015) *Energy-Efficient VCSELs for Optical Interconnects* (Springer, New York).
53. Chen YT, Karlsson KF, Birch J, Holtz PO (2016) Determination of critical diameters for intrinsic carrier diffusion-length of GaN nanorods with cryo-scanning near-field optical microscopy. *Sci Rep* 6:21482.
54. Peucheret C (2011) Note on Fabry-Perot interferometers (Dept of Photonics Engineering, Technical University of Denmark, Kongens Lyngby, Denmark).
55. Plis E, et al. (2011) Passivation of long-wave infrared InAs/GaSb strained layer superlattice detectors. *Infrared Phys Tech* 54(3):252–257.
56. Chang TH, et al. (2016) Selective release of InP heterostructures from InP substrates. *J Vac Sci Tech B* 34(4):041229.
57. Krishna S, Cavallo F, Klein B, Zamiri M (2016) US Patent 0023.0181-PCT.
58. Li X (2012) Metal assisted chemical etching for high aspect ratio nanostructures: A review of characteristics and applications in photovoltaics. *Curr Opin Solid State Mater Sci* 16(2):71–81.